

CORRELATION BETWEEN THE TOTAL GRAVITATING MASS OF GROUPS AND CLUSTERS AND THE SUPERMASSIVE BLACK HOLE MASS OF BRIGHTEST GALAXIES

ÁKOS BOGDAN¹, LORENZO LOVISARI¹, MARTA VOLONTERI², AND YOHAN DUBOIS²

¹Harvard Smithsonian Center for Astrophysics, 60 Garden Street, Cambridge, MA 02138, USA; abogdan@cfa.harvard.edu and

²Institut d'Astrophysique de Paris, Sorbonne Universités, UPMC Univ Paris 6 et CNRS, UMR 7095, 98 bis bd Arago, F-75014 Paris, France

Draft version January 11, 2018

ABSTRACT

Supermassive black holes (BHs) residing in the brightest cluster galaxies are over-massive relative to the stellar bulge mass or central stellar velocity dispersion of their host galaxies. As BHs residing at the bottom of the galaxy cluster's potential well may undergo physical processes that are driven by the large-scale characteristics of the galaxy clusters, it is possible that the growth of these BHs is (indirectly) governed by the properties of their host clusters. In this work, we explore the connection between the mass of BHs residing in the brightest group/cluster galaxies (BGGs/BCGs) and the virial temperature, and hence total gravitating mass, of galaxy groups/clusters. To this end, we investigate a sample of 17 BGGs/BCGs with dynamical BH mass measurements and utilize *XMM-Newton* X-ray observations to measure the virial temperatures and infer the M_{500} mass of the galaxy groups/clusters. We find that the $M_{\text{BH}} - kT$ relation is significantly tighter and exhibits smaller scatter than the $M_{\text{BH}} - M_{\text{bulge}}$ relations. The best-fitting power-law relations are $\log_{10}(M_{\text{BH}}/10^9 M_{\odot}) = 0.20 + 1.74 \log_{10}(kT/1 \text{ keV})$ and $\log_{10}(M_{\text{BH}}/10^9 M_{\odot}) = -0.80 + 1.72 \log_{10}(M_{\text{bulge}}/10^{11} M_{\odot})$. Thus, the BH mass of BGGs/BCGs may be set by physical processes that are governed by the properties of the host galaxy group/cluster. These results are confronted with the Horizon-AGN simulation, which reproduces the observed relations well, albeit the simulated relations exhibit notably smaller scatter.

Subject headings: galaxies: elliptical and lenticular, cD — galaxies: evolution — galaxies: halos — X-rays: galaxies — X-rays: ISM

1. INTRODUCTION

Observational studies of nearby galaxies demonstrated that galaxies of all morphology types host BHs at their center (for a review, see Kormendy & Ho 2013). By utilizing state-of-the-art telescopes and performing stellar kinematic or gas kinematic measurements of the nuclear regions of galaxies, accurate masses were derived for a sample of nearly 90 BHs. By correlating the BH mass with various properties of the host galaxies, the existence of scaling relations was established. Most notably, BH masses correlate with the velocity dispersion, stellar bulge mass, bulge luminosity, and dark matter halo mass (e.g. Magorrian et al. 1998; Gebhardt et al. 2000; Ferrarese 2002; Häring & Rix 2004; Gültekin et al. 2009; Beifiori et al. 2012; Vika et al. 2012; McConnell & Ma 2013; Läscher et al. 2014). The existence of these correlations suggests that the symbiotic growth of BHs and their host stellar bulges and dark matter halos plays a crucial role in galaxy evolution. Specifically, it is hypothesized that during the merger of two (spiral) galaxies, the energetic feedback from BHs can heat and expel the gas from the galaxy. This feedback could quench the active star formation and truncate the rapid growth phase of BHs (Silk & Rees 1998; King 2003; Wyithe & Loeb 2003; Hopkins et al. 2006). Alternatively, it may provide positive feedback and trigger star formation at high redshifts (Silk 2005; Pipino et al. 2009).

Although there is a general consensus about the importance of BHs in the evolution of galaxies, it remains ambiguous whether the growth of BHs are primarily driven by the stellar bulge or the dark matter

halo. Various observational and theoretical studies suggest that – at least in massive elliptical galaxies – the primary relation might be between BHs and the host dark matter halos (Ferrarese 2002; Bandara et al. 2009; Booth & Schaye 2010; Bogdán et al. 2012). However, the circular velocity, as a proxy for dark matter halo properties, is not a better predictor of BH mass with respect to velocity dispersion (Kormendy & Bender 2011; Volonteri et al. 2011; Sun et al. 2013). In low-mass, late-type and bulgeless galaxies, the looser correlation between the BH and dark matter halo may be a consequence of the inefficacy of low-mass galaxies in feeding the BHs, which in turn results in large scatter at the low-mass end of the relation (Volonteri et al. 2011; Dubois et al. 2015; Habouzit et al. 2016).

In this context, it is especially interesting to investigate BHs that reside at the bottom of the potential well of galaxy groups and clusters in BGGs/BCGs. These are among the most massive BHs ever detected, and curiously many of these BHs are over massive for the stellar bulge mass or central stellar velocity dispersion of their host BGG/BCG (Gebhardt et al. 2011; McConnell et al. 2011; Hlavacek-Larrondo et al. 2012; Ferré-Mateu et al. 2015; Savorgnan & Graham 2015). The preferential location of these BHs at the bottom of a deep potential well suggests that they may undergo a different evolutionary path than BHs in satellite galaxies. Specifically, centers of groups and clusters may retain a notable amount of gas that could be supplied to the BH after the star-formation has been quenched; cold gas from inflows could be directly fun-

TABLE 1
PROPERTIES OF THE STUDIED GALAXY GROUPS AND CLUSTERS

Galaxy name (1)	Distance (Mpc) (2)	N_{H} (10^{20} cm^{-2}) (3)	R_{500} (kpc) (4)	R_{frac} (5)	σ (km s^{-1}) (6)	kT (keV) (7)	M_{BH} ($10^9 M_{\odot}$) (8)	$\log M_{\text{bulge}}$ (M_{\odot}) (9)	M_{500} ($10^{13} M_{\odot}$) (10)
A1836-BCG	152.4 (a)	6.21	522	1.00	288 ± 14	1.351 ± 0.033	$3.74^{+0.42}_{-0.52}$ (d)	11.81 ± 0.10	4.05 ± 0.16
A3565-BCG	49.20 (a)	4.79	454	0.40	322 ± 16	1.051 ± 0.007	$1.30^{+0.20}_{-0.19}$ (d)	11.78 ± 0.09	2.68 ± 0.03
IC 1459	28.92 (b)	1.16	363	0.24	331 ± 5	0.696 ± 0.01	$2.48^{+0.48}_{-0.19}$ (e)	11.60 ± 0.09	1.36 ± 0.03
NGC 1316	20.95 (c)	2.56	393	0.22	226 ± 9	0.806 ± 0.006	$0.169^{+0.038}_{-0.030}$ (f)	11.84 ± 0.09	1.73 ± 0.02
NGC 1332	22.66 (b)	2.42	293	0.25	328 ± 9	0.473 ± 0.026	$1.47^{+0.41}_{-0.20}$ (g)	11.27 ± 0.09	0.72 ± 0.067
NGC 1407	29.00 (b)	6.85	459	0.19	276 ± 2	1.070 ± 0.005	$4.65^{+0.73}_{-0.41}$ (h)	11.74 ± 0.09	2.76 ± 0.25
NGC 1550	52.50 (a)	16.2	517	0.35	270 ± 10	1.329 ± 0.001	$3.87^{+0.61}_{-0.71}$ (h)	11.33 ± 0.09	3.95 ± 0.05
NGC 3091	53.02 (a)	4.68	400	0.48	297 ± 12	0.835 ± 0.011	$3.72^{+0.11}_{-0.51}$ (h)	11.61 ± 0.09	1.83 ± 0.04
NGC 3585	20.51 (b)	6.41	247	0.33	213 ± 11	0.347 ± 0.008	$0.329^{+0.145}_{-0.058}$ (i)	11.26 ± 0.09	0.43 ± 0.17
NGC 3607	22.65 (b)	1.44	306	0.15	229 ± 11	0.512 ± 0.026	$0.137^{+0.045}_{-0.047}$ (i)	11.26 ± 0.09	0.082 ± 0.07
NGC 3842	92.20 (a)	1.67	942	0.32	270 ± 27	3.963 ± 0.065	$9.09^{+2.34}_{-2.81}$ (j)	11.77 ± 0.09	23.90 ± 0.70
NGC 4291	26.58 (b)	3.26	358	0.24	242 ± 12	0.682 ± 0.002	$0.978^{+0.308}_{-0.308}$ (k)	10.85 ± 0.09	1.31 ± 0.05
NGC 4486	16.68 (c)	2.11	647	0.09	324^{+28}_{-12}	1.997 ± 0.001	$6.15^{+0.38}_{-0.37}$ (l)	11.72 ± 0.09	7.73 ± 0.01
NGC 4889	102.0 (a)	0.87	1395	0.24	347 ± 5	8.165 ± 0.037	$20.80^{+15.80}_{-15.90}$ (j)	12.09 ± 0.09	78.90 ± 0.60
NGC 6251	108.4 (a)	7.33	334	1.00	290 ± 14	0.598 ± 0.049	$0.614^{+0.204}_{-0.205}$ (m)	11.88 ± 0.09	1.06 ± 0.15
NGC 7052	70.40 (a)	13.8	387	0.59	266 ± 13	0.785 ± 0.023	$0.396^{+0.276}_{-0.156}$ (n)	11.61 ± 0.10	1.66 ± 0.08
NGC 7619	53.85 (b)	6.26	442	0.41	292 ± 5	0.997 ± 0.005	$2.30^{+1.15}_{-0.11}$ (h)	11.65 ± 0.09	2.46 ± 0.02

Columns are as follows: (1) Name of the BGG/BCG; (2) Distance to the galaxy. References are: (a) Kormendy & Ho (2013); (b) Tonry et al. (2001); (c) Blakeslee et al. (2009); (3) Line-of-sight column density toward the galaxy (Willingale et al. 2013); (4) R_{500} radius of the group/cluster; (5) Fraction of the R_{500} radius that is included within the *XMM-Newton* FOV; (6) Central stellar velocity dispersion of the BGG/BCG taken from Kormendy & Ho (2013); (7) Best-fit temperature of the hot X-ray emitting gas; (8) BH mass obtained through dynamical modeling. References are: (d) Dalla Bontà et al. (2009); (e) Cappellari et al. (2002); (f) Nowak et al. (2008); (g) Rusli et al. (2011); (h) Rusli et al. (2013); (i) Gültekin et al. (2009); (j) McConnell et al. (2012); (k) Schulze & Gebhardt (2011); (l) Gebhardt et al. (2011); (m) Ferrarese & Ford (1999); (n) van der Marel & van den Bosch (1998); (9) Stellar bulge mass taken from Kormendy & Ho (2013); (10) M_{500} mass inferred from the best-fit gas temperature given in column (5), and the $kT - M_{500}$ scaling relation established in Lovisari et al. (2015). The errors associated with M_{500} were computed from the temperature uncertainties.

neled onto the center of the group/cluster and directly feed the BHs; or low angular momentum mergers – that are believed to form the most massive galaxies – may play a role in increasing the BH mass. Because these processes occur in centers of groups/clusters and likely depend on the large-scale characteristics of the group/cluster, it is sensible to probe whether there is a correlation between the BH mass of BGGs/BCGs and the large-scale properties, such as gas temperature or M_{500} mass¹, of the host groups and clusters. To probe the existence of such a correlation, we rely on dynamically measured BHs and utilize *XMM-Newton* X-ray observations to characterize the dark matter halo properties.

The paper is structured as follows. In Section 2 we introduce the analyzed sample and our selection criteria. In Section 3 we discuss the analysis of the *XMM-Newton* data. Our results are presented in Section 4, where we derive the best-fit gas temperatures, compute the M_{500} mass, and investigate the tightness of the $M_{\text{BH}} - kT$, $M_{\text{BH}} - M_{500}$ and $M_{\text{BH}} - M_{\text{bulge}}$ relations. In Section 5 we place our results in context and compare the observed relations with those obtained from the Horizon-AGN simulations. Our results are summarized in Section

6. In this work, we assume $H_0 = 70 \text{ km s}^{-1} \text{ Mpc}^{-1}$, $\Omega_M = 0.3$, and $\Omega_{\Lambda} = 0.7$, and all error bars represent 1σ uncertainties.

2. SAMPLE SELECTION

As we aim to explore the connection between the BH mass of BGGs/BCGs and the M_{500} of galaxy groups/clusters, we require accurate measurements of these quantities. While the M_{500} of groups and clusters can be derived from relatively short X-ray observations, measuring BH masses using dynamical methods requires state-of-the-art optical telescopes and complex modeling. Therefore, dynamical BH mass measurement are limited to the most massive and/or nearby BHs. As a consequence, only 88 BH masses were measured using dynamical methods until recently (Kormendy & Ho 2013). This set of BHs represents our initial sample.

From the 88 BHs with dynamical mass measurements, we select those that reside in early-type (E/S0) galaxies, whose systems are typically the BGGs/BCGs of galaxy groups and clusters. This limits our sample to 45 ellipticals and 20 S0 galaxies. Then we utilize the galaxy group and cluster catalog of Tully (2015) and search for those BHs that reside at the center of galaxy groups/clusters, i.e. are BGG/BCGs. We identified 36 such galaxies, implying that the remaining 29 E/S0 galaxies are satellites.

To derive the M_{500} mass of groups and clusters, we use X-ray scaling relations established between the aver-

¹ The radius r_{500} is the radius of a sphere where the mean mass density is $500\rho_{\text{crit}}$, where ρ_{crit} is the critical density of the universe. The mass enclosed within r_{500} is M_{500} .

age gas temperature of the hot intragroup/intracluster medium and the M_{500} mass of the group/cluster (Lovisari et al. 2015). To measure the X-ray gas temperatures, we utilize X-ray data taken with the *XMM-Newton* observatory. These observations are ideal to study the hot gas for two reasons. First, the 30' field-of-view (FOV) of *XMM-Newton* allows to explore the galaxy groups/clusters out to a significant fraction of their r_{500} radius. Second, due to the large collecting area of the *XMM-Newton* cameras, relatively short observations are sufficient to accurately measure the average gas temperature. Therefore, we searched the *XMM-Newton* archive and found that 22 of these groups and clusters have publicly available X-ray observations.

From this sample, we excluded two bright radio galaxies, Centaurs A and Cygnus A, whose X-ray emission is disrupted by the radio jets, implying that the X-ray scaling relations cannot be applied. From the remaining 20 galaxy groups/clusters we found that the galaxy groups associated with NGC 1194, NGC 2787, and NGC 2960 do not have large-scale diffuse X-ray emission. However, these relatively low stellar mass galaxies ($M_{\text{bulge}} \lesssim 10^{11} M_{\odot}$) reside in the center of poor groups and host low-mass ($M_{\text{BH}} < 10^8 M_{\odot}$) BHs. Therefore, the gravitational potential of these groups may be too shallow to retain a significant amount of hot X-ray gas. In these systems, the faint X-ray emission originates from the optical body of the BGGs. As measuring the X-ray properties of the galaxy gas in these systems would not represent the properties of the large-scale dark matter halo of the groups, we exclude these systems from our analysis. Thus, our final sample consists of 17 groups and clusters. We stress that the BH mass of the sample galaxies were obtained using either stellar or ionized gas dynamics, and our sample does not include any water maser measurements. The properties of the sample are listed in Table 1.

3. ANALYSIS OF THE *XMM-NEWTON* DATA

The groups and clusters in our sample were observed with the European Photon Imaging Camera (EPIC) aboard *XMM-Newton*. Details about the observations are listed in Table 1. To analyze the data, we utilized the XMM Science Analysis System (SAS) version 16.0.0 and Current Calibration Files (CCF).

We analyzed the data following the main steps described in Lovisari et al. (2015). First, we applied *emchain* and *epchain* to the raw data, which tasks generated calibrated event files. For the analysis, we included event patterns 0-12 for EPIC-MOS and 0 for EPIC-PN data. We also removed bright pixels and hot columns and applied out-of-time correction for the EPIC-PN data.

Given that the *XMM-Newton* observations may be severely affected by high background periods, we applied a two-step filtering process. First, we constructed a light curve using 100 s binning in the 10 – 12 keV and 12 – 14 keV bands for EPIC-MOS and EPIC-PN, respectively. By applying 2σ clipping, we generated a good-time-interval file and excluded the high background periods from the event files. Second, we built light curves using the cleaned event files using 10 s binning in the 0.3 – 10 keV band. Similarly, we applied 2σ clipping to identify and remove any potentially remaining high background periods. Given that the detector characteris-

TABLE 2
EXPOSURE TIMES OF THE ANALYZED *XMM-Newton* OBSERVATIONS

Galaxy name	$t_{\text{total}}^{\dagger}$ (ks)	$t_{\text{clean}}^{\ddagger}$ (ks)
A1836-BCG	36.1/36.2/30.3	20.3/22.6/12.4
A3565-BCG	70.6 70.7 60.9	30.6/33.7/19.5
IC 1459	131.4/131.9/114.6	83.5/82.5/64.6
NGC 1316	106.1/106.1/89.4	54.7/56.7/28.9
NGC 1332	64.7/64.8/56.1	49.2/50.1/41.1
NGC 1407	64.4/65.3/47.2	33.6/34.2/24.5
NGC 1550	89.5/87.8/74.1	45.5/48.3/29.5
NGC 3091	20.9/20.9/16.5	18.4/18.7/14.5
NGC 3585	20.9/20.7/16.5	10.8/10.9/7.3
NGC 3607	43.7/43.7/38.1	25.1/26.2/17.1
NGC 3842	24.2/24.3/16.6	21.3/21.5/13.5
NGC 4291	50.4/50.4/15.3	28.4/32.2/13.2
NGC 4486	69.4/68.4/53.9	69.4/68.4/53.9
NGC 4889	25.0/25.0/18.4	18.5/19.2/14.3
NGC 6251	49.3/49.4/40.9	6.8/11.0/2.0
NGC 7052	34.2/34.2/28.6	15.8/16.6/12.9
NGC 7619	40.5/40.5/35.4	35.6/34.7/28.3

\dagger Total exposure time taken with EPIC MOS1, MOS2, and PN cameras, respectively.

\ddagger The clean exposure times refer for the EPIC MOS1, MOS2, and PN cameras, respectively.

tics of EPIC-MOS and EPIC-PN are different, EPIC-PN is significantly more sensitive to high background periods. As a consequence, the clean EPIC-PN exposure time is typically much shorter than that for EPIC-MOS. The resulting total clean exposure time for each analyzed galaxy group and cluster is listed in Table 2.

In this work, we aim to study the diffuse emission associated with galaxy groups and clusters. Therefore, it is essential to identify and exclude bright point sources (mostly background AGN) from the study. To this end, we utilized the task *ewavelet* on the 0.3 – 10 keV band images, which produced a list of point sources. Because the source detection algorithm often identifies the luminous cores of groups and clusters as point sources, we checked the source lists by eye and removed these detections. The thus obtained source regions were masked from the further analysis of the diffuse emission.

An essential part of the data analysis is to precisely account for the particle and cosmic X-ray background (CXB) components. While the influence of background is less pronounced in luminous galaxy clusters, a predominant fraction of our sample consists of relatively faint galaxy groups. Moreover, all systems in our sample fill the entire FOV of the *XMM-Newton* cameras, which further complicates the accurate background subtraction. To account for the quiescent and non-vignetted particle background components, we utilized the filter-wheel closed observations for the EPIC-MOS and EPIC-PN data (Freyberg et al. 2006; Snowden et al. 2008). These data were re-normalized using the count rates observed in the 3 – 10 keV energy range (Zhang et al. 2009). This re-normalized filter-wheel closed observation was used to

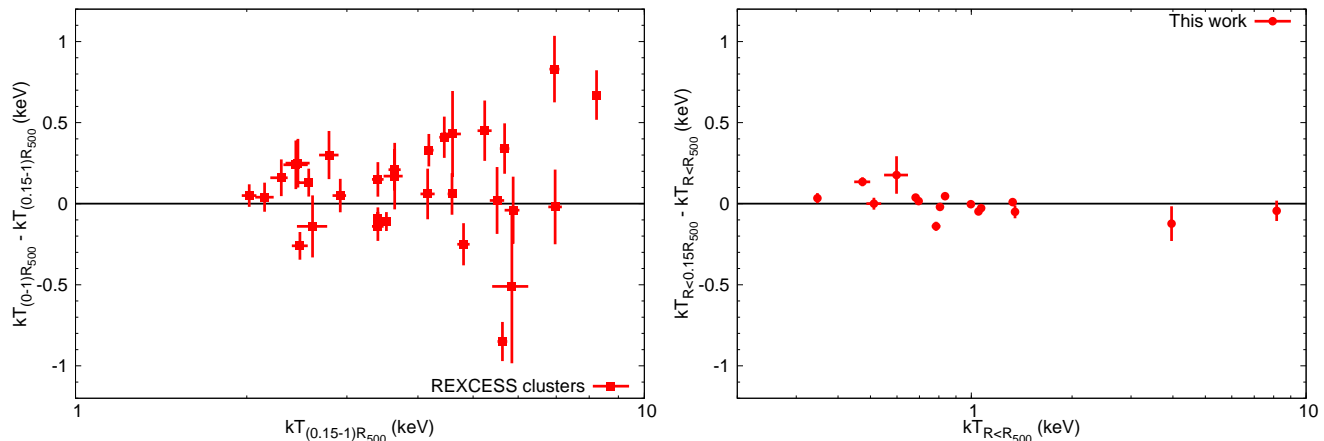


FIG. 1.— Spectroscopic gas temperatures measured in different radial regions. To highlight any offsets, on the y-axis we show the difference between the best-fit gas temperatures. The solid line shows the one-to-one relations. In the left panel, we show the gas temperatures for 31 galaxy clusters from the Representative *XMM-Newton* Cluster Structure Survey (Pratt et al. 2009). This relation shows that the best-fit average temperatures are virtually identical if the core region ($R < 0.15R_{500}$) of the clusters is included or excised. In the right panel, we show the best-fit gas temperatures measured for the groups and clusters analyzed in this work. The results – in agreement with those presented in the left panel – show that the gas temperatures are nearly identical if they are measured within $< 0.15R_{500}$ or within a larger region defined by the *XMM-Newton* FOV.

subtract the instrumental background components. The emission originating from the cosmic X-ray background was included in the spectral fits. Specifically, we used the spectra from the ROSAT All Sky Survey data that were obtained through the HEASARC webpage². The CXB spectra were extracted from regions beyond the virial radius of the groups/clusters; hence, in these regions, we do not expect significant emission associated with these systems. We describe the spectrum of the CXB with a three-component model including an absorbed ~ 0.2 keV thermal model, an unabsorbed ~ 0.1 keV thermal component, and a power-law model with a slope of $\Gamma = 1.41$. The temperature of the thermal models describing the CXB were allowed to vary, but their metallicity was fixed at 1.0 solar. This model for the CXB was simultaneously fit with the source spectra extracted from the three cameras. For the fitting, the temperature and the metallicities of the hot group/cluster gas were allowed to vary, but they were linked for the three EPIC cameras.

4. RESULTS

4.1. Measuring the gas temperatures

To probe the total gravitating mass of the galaxy groups and clusters in our sample, we rely on *XMM-Newton* X-ray observations of the hot gas. Although it would be desirable to compute the total gravitating mass of the groups/clusters by assuming that the hot X-ray gas is in hydrostatic equilibrium, this would require accurate measurements of the density and temperature profiles, preferably out to R_{500} . The relatively X-ray faint nature of several groups in our sample, the short exposure times of the *XMM-Newton* observations, and the *XMM-Newton* FOV that is smaller than the actual R_{500} make it unfeasible to build temperature profiles for most systems in our sample. However, under the assumption of hydrostatic equilibrium, the virial temperature of the intragroup or intracluster medium is directly proportional with the total mass of the system (Pratt et al.

2009; Eckmiller et al. 2011; Lovisari et al. 2015). Thus, we rely on the temperature of the intragroup/intracluster medium to trace the total mass of the groups/clusters.

Because all groups/clusters in our sample are relatively nearby ($D \lesssim 150$ Mpc), their r_{500} radius is comparable or exceeds the *XMM-Newton* FOV. Therefore, we extract spectra from circular regions centered on the center of the groups/clusters, whose radii approximately fill the FOV. Given the different virial radii and the different distance of the groups/clusters, the extraction regions vary in the range of $(0.09 - 1)R_{500}$ (see Table 1).

For each system, we fit the X-ray spectra with an optically-thin thermal plasma emission model (APEC model in XSPEC). The metal abundances were free to vary (Asplund et al. 2009) and the column density was fixed at the total column density that includes both the atomic and molecular hydrogen (Willingale et al. 2013). Because we extract three spectra from the EPIC cameras, we fit these spectra simultaneously. For most systems in our sample, the X-ray emission from the intragroup/intracluster medium dominates the overall emission. However, in a few fainter galaxy groups, the emission from the central galaxy may add a noticeable contribution, particularly at energies exceeding 2 keV. In these cases, we added a power-law model to account for the emission originating from the population of unresolved X-ray binaries (Gilfanov 2004) that are associated with the BGG. For the power-law model, we fixed the slope at $\Gamma = 1.56$, which is the average slope of low-mass X-ray binaries (Irwin et al. 2003). We note that adding a power-law component did not change the best-fit gas temperature, but it improved the overall goodness of the fits. The best-fit gas temperatures are listed in Table 1.

4.2. Temperature dependence as a function of extraction radius

In this work, we use the $kT - M_{500}$ scaling relation to derive the M_{500} of the groups/clusters in our sample. However, the average gas temperatures presented in Lovisari et al. (2015) were obtained from the cool-

² <http://heasarc.gsfc.nasa.gov/cgi-bin/Tools/xraybg/xraybg.pl>

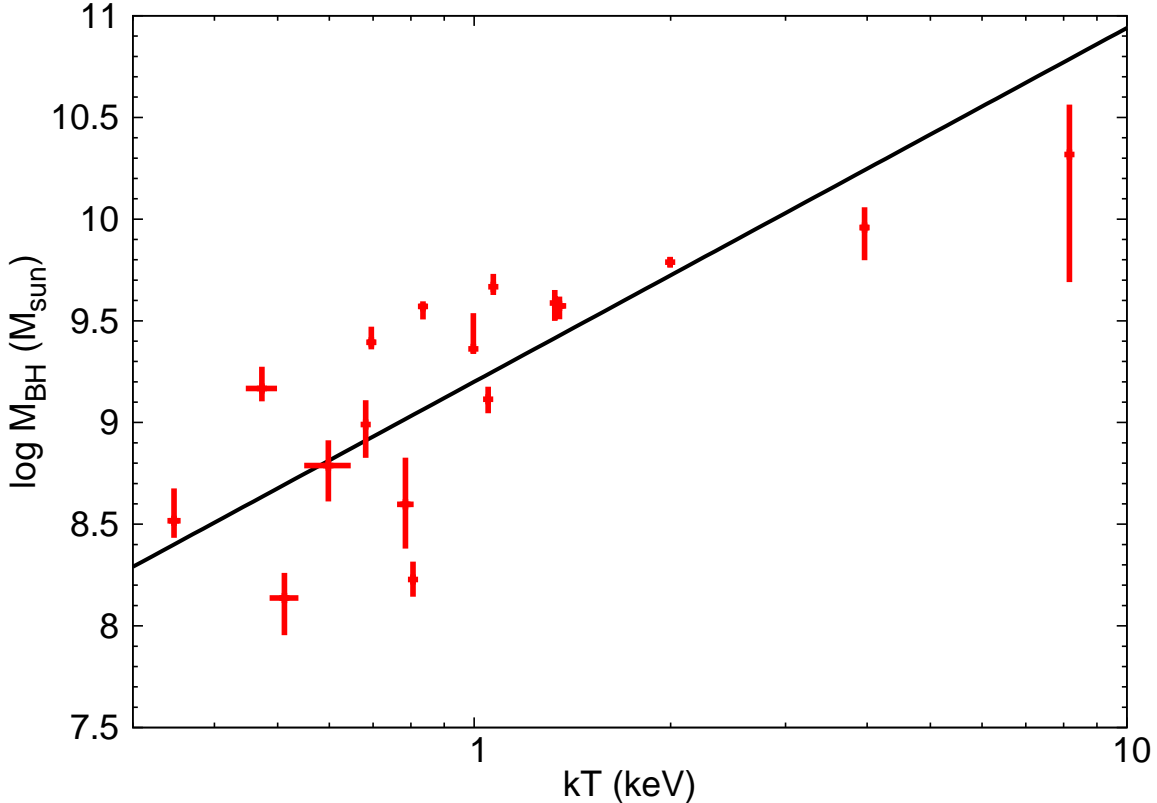


FIG. 2.— Correlation between the BH mass and the best-fit gas temperature of the group/clusters. Note that the gas temperature of the intragroup/intracluster medium is a direct tracer of the total gravitation mass (Eckmiller et al. 2011; Lovisari et al. 2015). Our sample covers a broad range of systems, including low-mass groups with sub-keV temperatures and massive, ~ 8 keV, galaxy clusters. The solid line shows the best-fit power-law relation that can be described as $\log_{10}(M_{\text{BH}}/10^9 M_{\odot}) = 0.20 + 1.74 \log_{10}(kT/1 \text{ keV})$. The Pearson and Spearman correlation coefficients of the relation are 0.97 and 0.83, respectively, showing a strong correlation.

core excised spectra and refer to the radial region of $(0.15 - 1)R_{500}$. The different extraction region applied by Lovisari et al. (2015) has two main origins. First, the groups in their sample were – on average – more distant; hence, a larger fraction of them could fit in the *XMM-Newton* FOV. Second, they excised the central regions of the groups to exclude any potential cool cores. Given the proximity of the groups/clusters in our sample and the *XMM-Newton* FOV, it is not feasible to probe the characteristics of the X-ray gas out to R_{500} . To map the intragroup/intracluster medium of these systems out to R_{500} , extensive mosaic X-ray observations would be required. However, such observations are not available in the archive; therefore, we must restrict our study to the regions that are included within the *XMM-Newton* FOV. In addition, for NGC 3607 and NGC 4486 only the innermost regions ($R < 0.15R_{500}$) are included within the FOV (Table 1). Given that we derive the M_{500} masses from the best-fit gas temperature, we must investigate whether the temperatures exhibit a notable variation if different extraction regions are used. To probe the temperature variations as a function of radius, we use multiple approaches.

First, we investigate the temperature profiles of the galaxy groups studied in Lovisari et al. (2015). Those temperature profiles, which can be approximated with the self-similar temperature profile of Vikhlinin et al. (2006), exhibit the peak temperatures at $\sim 0.1R_{500}$ and level off at larger radii. For most systems the temper-

ature difference between the peak temperature and the lowest temperatures reached in the outskirts is $\lesssim 30\%$. This value should be considered as an upper limit on the temperature uncertainty, as the best-fit temperatures for our sample galaxies are luminosity-weighted values computed from regions, which include the peak and part of the flattening profile.

Second, we utilize the results of Pratt et al. (2009), who investigated 31 galaxy clusters from the Representative *XMM-Newton* Cluster Structure Survey (REXCESS). These authors measured the gas temperature in three different regions: $(0 - 1)R_{500}$, $(0.15 - 1)R_{500}$, and $(0.15 - 0.75)R_{500}$. In the left panel of Figure 1 we present the scatter plot showing the best-fit temperatures obtained between $R < R_{500}$ and $(0.15 - 1)R_{500}$. This plot demonstrates that the average gas temperatures are virtually identical whether they are measured at radii $R < 0.15R_{500}$ or $(0.15 - 1)R_{500}$. Thus, based on the results obtained for the REXCESS sample, it appears unlikely that including or excluding the innermost regions of groups/clusters will significantly influence the overall temperatures. To further confirm this, we compared the gas temperatures for two different regions for the groups and clusters in our sample. Namely, we extracted spectra from $R < 0.15R_{500}$ and from the full apertures. In the right panel of Figure 1 we show the scatter plot obtained between these two temperatures and we tabulate the best-fit values in Table 3. This reveals that the temperatures are nearly uniform and do not show a notable

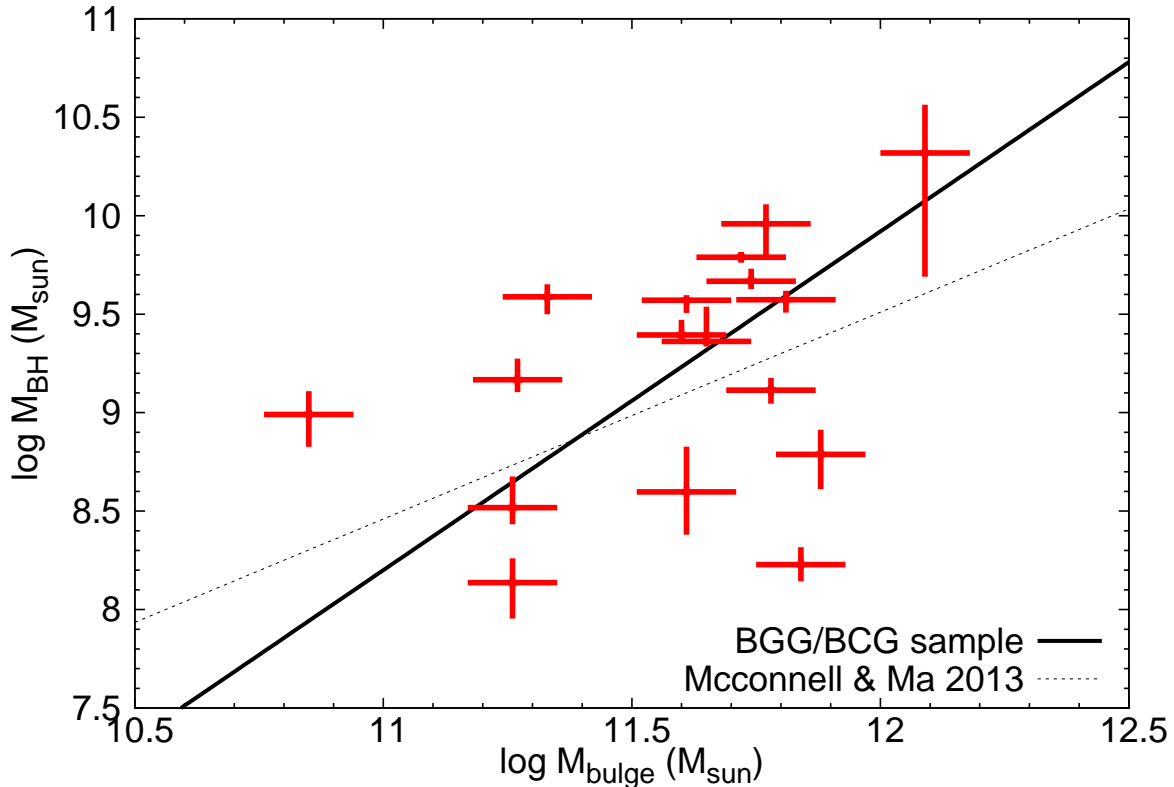


FIG. 3.— Correlation between the BH mass and the stellar bulge mass of BGGs/BCGs. Thick solid line shows the best-fit power-law relation to the 17 data points studied in this work. The best-fit relation is $\log_{10}(M_{\text{BH}}/10^9 M_{\odot}) = -0.80 + 1.72 \log_{10}(M_{\text{bulge}}/10^{11} M_{\odot})$. The dashed line shows the best-fit relation obtained for a sample of 72 galaxies with dynamical BH masses (McConnell & Ma 2013). Most BGGs/BCGs host over-massive BHs relative to this relation. We note that all 17 BGGs/BCGs that are studied in the current work were included in the study of McConnell & Ma (2013). The Pearson and Spearman correlation coefficients of the best-fit relation are 0.70 and 0.35, respectively, showing a moderate/weak correlation.

variation whether the innermost $R < 0.15R_{500}$ region is excised.

Third, we investigated six galaxy groups/clusters from our sample, which are sufficiently distant and allow us to extract spectra and measure temperatures out to $\geq 0.4R_{500}$. Specifically, we selected Abell 1836, Abell 3565, NGC 3091, NGC 7052, NGC 6251, and NGC 7619. For each of these systems, we extracted spectra within the radii $R < 0.1R_{500}$, $R < 0.2R_{500}$, $R < 0.3R_{500}$, and $R < 0.4R_{500}$. We fit the spectra following the method described in Section 4.1 and measured the gas temperatures in each of these regions. The results point out that the temperatures measured within these radii agree within 10%.

Thus, we conclude that measuring the temperatures of the intragroup/intracluster medium within radii that are primarily defined by the FOV will not influence our conclusions in any significant way. Specifically, it may add a systematic uncertainty of no more than 10%. This uncertainty in the gas temperature corresponds to a $\leq 20\%$ systematic uncertainty in the inferred M_{500} values.

4.3. Measuring M_{500}

Based on the obtained gas temperatures, we infer M_{500} by utilizing the $kT - M_{500}$ scaling relation from Lovisari et al. (2015):

$$M_{500} = 7.744 \times 10^{13} (kT/2 \text{ keV})^{1.65} M_{\odot} .$$

The slope and normalization of this relation is in good agreement with that obtained for more massive clusters; hence, the Lovisari et al. (2015) relation is essentially the extension of the $kT - M_{500}$ relation established for clusters (e.g. Arnaud et al. 2005). The results presented in Lovisari et al. (2015) demonstrate that the $kT - M_{500}$ relation can be extended to the lower-mass end of groups. Thus, the gas temperatures of the groups/clusters obtained in this work can be robustly used to determine their total gravitating mass.

Based on the best-fit temperatures, we obtained M_{500} masses in the range of $(0.43 - 78.90) \times 10^{13} M_{\odot}$; hence, our sample groups and clusters cover more than two orders of magnitude in M_{500} . The values for each system are given in tabulated form in Table 1.

4.4. Correlations

Based on the dynamical BH mass measurements (see Table 1), the stellar bulge masses (taken from Kormendy & Ho 2013), and the best-fit temperatures measured for the groups/clusters, we investigate the following three relations: $M_{\text{BH}} - kT$, $M_{\text{BH}} - M_{\text{bulge}}$, $M_{\text{bulge}} - kT$. We fit each of these relations in log space using the functional form of:

$$\log_{10} Y = \alpha + \beta \log_{10} X ,$$

where α and β represents the intercept and the slope, respectively, and X and Y are given in units of

TABLE 3
BEST-FIT GAS TEMPERATURES EXTRACTED FROM VARIOUS REGIONS

Galaxy name	kT ($R \leq R_{500}$) (keV)	kT ($R < 0.15R_{500}$) (keV)
1836-BCG	1.351 ± 0.033	1.301 ± 0.022
A3565-BCG	1.051 ± 0.007	1.003 ± 0.007
IC 1459	0.696 ± 0.01	0.712 ± 0.007
NGC 1316	0.806 ± 0.006	0.786 ± 0.004
NGC 1332	0.473 ± 0.026	0.608 ± 0.008
NGC 1407	1.070 ± 0.005	1.043 ± 0.005
NGC 1550	1.329 ± 0.001	1.339 ± 0.002
NGC 3091	0.835 ± 0.011	0.881 ± 0.008
NGC 3585	0.347 ± 0.008	0.381 ± 0.030
NGC 3607 [†]	0.512 ± 0.026	—
NGC 3842	3.963 ± 0.065	3.840 ± 0.085
NGC 4291	0.682 ± 0.002	0.720 ± 0.009
NGC 4486 [†]	1.997 ± 0.001	—
NGC 4889	8.165 ± 0.037	8.121 ± 0.051
NGC 6251	0.598 ± 0.049	0.775 ± 0.105
NGC 7052	0.785 ± 0.023	0.646 ± 0.016
NGC 7619	0.997 ± 0.005	0.994 ± 0.004

[†] Note that NGC 3607 and NGC 4486 can only be explored to $0.15R_{500}$ and $0.09R_{500}$, respectively. Therefore, it is not feasible to perform the comparison for these two objects.

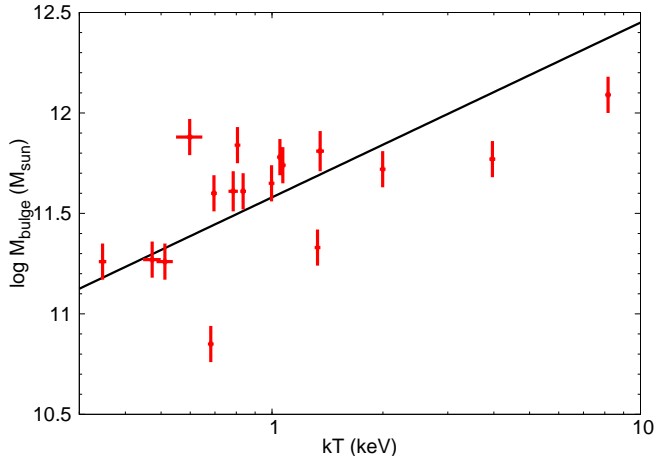


FIG. 4.— Stellar bulge mass as a function of gas temperature for a sample of 17 systems studied in this work. The solid line shows the best-fit relation that can be described as $\log_{10}(M_{\text{bulge}}/10^9 M_{\odot}) = 0.58 + 0.87 \log_{10}(kT/1 \text{ keV})$. The Pearson and Spearman correlation coefficients of the relation are 0.73 and 0.60, showing a moderate correlation.

$M_{\text{BH}}/(10^{11} M_{\odot})$, $kT/(1 \text{ keV})$, and $M_{\text{bulge}}/(10^{11} M_{\odot})$.

We used the BCES.REGRESS code to perform the linear regression and to derive the intrinsic scatter in the relations (Akritas & Bershady 1996). We computed the fits in log-log space using the bisector fitting method of the BCES code. The logarithm scatter, σ_X and σ_Y , along the X- and Y-axis were computed following the formalism described in Lovisari et al. (2015). The best-

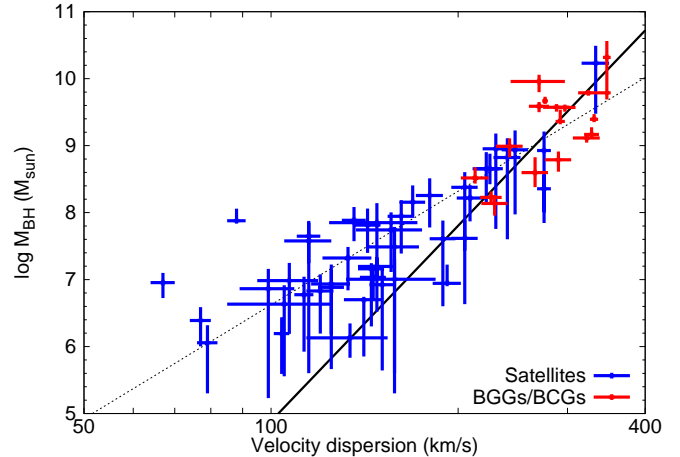


FIG. 5.— BH mass as a function of velocity dispersion for the 17 BGGs/BCGs in our sample and all galaxies with dynamical BH mass measurements (Kormendy & Ho 2013). The thick solid line shows the best-fit relation for the BGGs/BCGs, whereas the dashed line shows the best-fit relation from McConnell & Ma (2013). Note that the BGG/BCG sample produces a steeper relation than that obtained for the entire BH sample.

fit parameters and the scatter of the fits are listed in Table 4. The obtained scaling relations are the following:

$$\log_{10} \left(\frac{M_{\text{BH}}}{10^9 M_{\odot}} \right) = 0.20 + 1.74 \log_{10} \left(\frac{kT}{1 \text{ keV}} \right)$$

$$\log_{10} \left(\frac{M_{\text{BH}}}{10^9 M_{\odot}} \right) = -0.22 + 1.07 \log_{10} \left(\frac{M_{500}}{10^{13} M_{\odot}} \right)$$

$$\log_{10} \left(\frac{M_{\text{BH}}}{10^9 M_{\odot}} \right) = -0.80 + 1.72 \log_{10} \left(\frac{M_{\text{bulge}}}{10^{11} M_{\odot}} \right)$$

$$\log_{10} \left(\frac{M_{\text{BH}}}{10^9 M_{\odot}} \right) = 0.51 + 9.68 \log_{10} \left(\frac{\sigma}{300 \text{ km s}^{-1}} \right)$$

$$\log_{10} \left(\frac{M_{\text{bulge}}}{10^{11} M_{\odot}} \right) = 0.58 + 0.87 \log_{10} \left(\frac{kT}{1 \text{ keV}} \right)$$

We depict the observed data points with the best-fit relations in Figures 2, 3, and 4.

The results of the linear regression point out that the $M_{\text{BH}} - kT$ relation (Figure 2) is significantly tighter than the $M_{\text{BH}} - M_{\text{bulge}}$ relation (Figure 3). In addition, we probe the tightness of the relations by computing the Pearson and Spearman correlation coefficients. These point out a strong correlation for the $M_{\text{BH}} - kT$ relation ($r = 0.95$, $\rho = 0.83$) and a weak correlation for the $M_{\text{BH}} - M_{\text{bulge}}$ relation ($r = 0.70$, $\rho = 0.35$). Thus, in the sample of 17 galaxy groups/clusters the BH mass traces the gas temperature significantly more tightly than the stellar bulge mass.

We also probe $M_{\text{bulge}} - kT$ to test whether the stellar bulge mass and the gas temperature of the groups/clusters exhibit a tight correlation (Figure 4). We find that the scatter of this relation exceeds that of the $M_{\text{BH}} - kT$ relation, and the Pearson and Spearman correlation coefficients denote a moderate correlation (Table

TABLE 4
BEST-FIT PARAMETERS ON LINEAR REGRESSION

Relation	α	β	σ_X	σ_Y	r^\dagger	ρ^\ddagger
$M_{\text{BH}} - kT$	0.20 ± 0.09	1.74 ± 0.16	0.22	0.38	0.97	0.83
$M_{\text{BH}} - M_{500}$	-0.22 ± 0.13	1.07 ± 0.17	0.36	0.38	0.97	0.83
$M_{\text{BH}} - M_{\text{bulge}}$	-0.80 ± 0.23	1.72 ± 0.27	0.35	0.61	0.70	0.35
$M_{\text{BH}} - \sigma$	0.51 ± 0.11	9.68 ± 0.15	0.05	0.46	0.51	0.58
$M_{\text{bulge}} - kT$	0.58 ± 0.07	0.87 ± 0.24	0.30	0.26	0.73	0.60
$M_{\text{BH}} - M_{500}$ (simulated)	-0.05 ± 0.01	0.92 ± 0.06	0.20	0.19	0.82	0.84

† Pearson correlation coefficient

‡ Spearman correlation coefficient

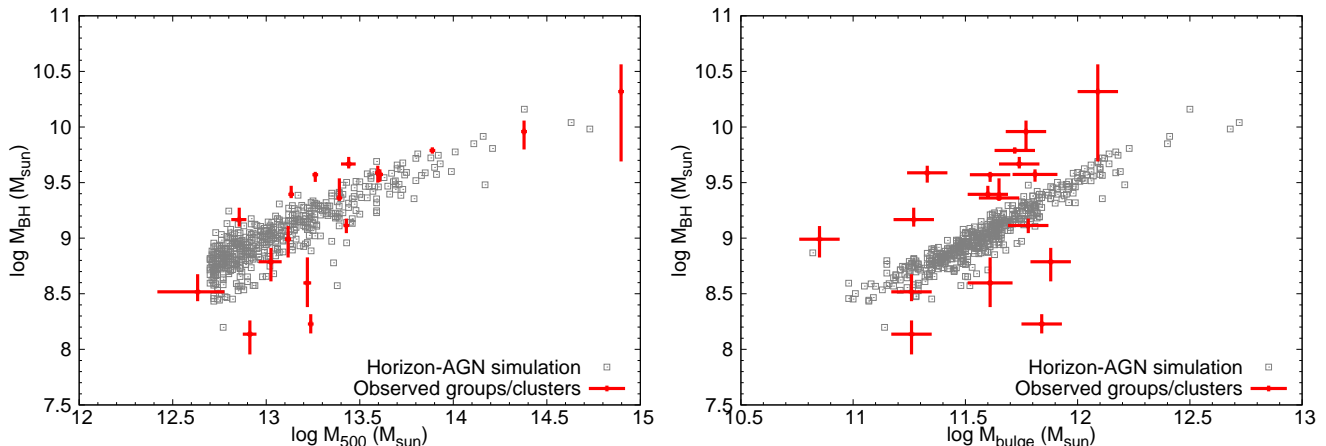


FIG. 6.— Left: BH mass as a function of M_{500} (left panel) and M_{bulge} (right panel). In these panels, the observed data for the sample of 17 galaxy groups/clusters is compared with the groups/clusters from the the Horizon-AGN simulations. There is an overall good agreement between the observed and simulated relations. However, the simulated relations, especially the $M_{\text{BH}} - M_{\text{bulge}}$ exhibit smaller scatter than the observed ones.

4). This suggests that the tight correlation between the BH mass and group/cluster temperature is not the consequence of – an even tighter – relation between the stellar bulge mass and the group/cluster temperature.

In Figure 5, we show the $M_{\text{BH}} - \sigma$ relation for the 17 BGGs/BCGs and extend the sample with galaxies with dynamical BH masses. To this end, we utilized the BH catalog compiled by Kormendy & Ho (2013), which includes additional 69 galaxies. We find that the best-fit $M_{\text{BH}} - \sigma$ relation exhibits a significantly steeper slope than the relation established for the full galaxy sample.

5. DISCUSSION

5.1. The Horizon-AGN simulation

We compare our results to the Horizon-AGN simulation (Dubois et al. 2014). This simulation is run with the Adaptive Mesh Refinement code RAMSES (Teyssier 2002) and includes prescriptions for background UV heating, gas cooling including the contribution from metals released by stellar feedback, star formation following a Schmidt law with a 1 per cent efficiency (Rasera & Teyssier 2006), and feedback from stellar winds and type Ia and type II supernovae (SNaE) assuming a Salpeter initial mass function (Dubois & Teyssier 2008; Kaviraj et al. 2017). BH formation, accretion, and feedback are included in the simulation. The accretion onto BHs follows the Bondi-

Hoyle-Lyttleton rate, capped at the Eddington luminosity with an assumed radiative efficiency of $\epsilon_r = 0.1$. AGN feedback is a combination of two different modes: for $\dot{M}_{\text{BH}}/\dot{M}_{\text{Edd}} > 0.01$, an isotropic injection of thermal energy into the gas within a sphere of radius $\Delta x = 1$ proper kpc (corresponding to the simulation effective resolution), at an energy deposition rate: $\dot{E}_{\text{AGN}} = \epsilon_f \epsilon_r \dot{M}_{\text{BH}} c^2$, where $\epsilon_f = 0.15$ was chosen to reproduce the correlations between BHs and galaxies and the BH density in our local universe (see Dubois et al. 2012). At low accretion rates, $\dot{M}_{\text{BH}}/\dot{M}_{\text{Edd}} < 0.01$, AGN feedback energy, with $\epsilon_f = 1$, is deposited into a bipolar outflow with a jet velocity of 10^4 km s^{-1} into a cylinder with a cross section of radius Δx and height $2 \Delta x$ following (Omma et al. 2004). Further details about the jet implementation are given in Dubois et al. 2010.

We identify dark matter halos and sub-halos using HaloMaker, which uses AdaptaHOP (Aubert et al. 2004; Tweed et al. 2009), a structure-finder based on the identification of saddle points in the (smoothed) density field, using the shrinking sphere approach proposed by Power et al. (2003) to determine the halo center. Only dark matter halos identified with more than 50 particles are considered. Galaxies are identified using the same method and same parameters but using the stellar particle distribution instead of the dark matter one. We as-

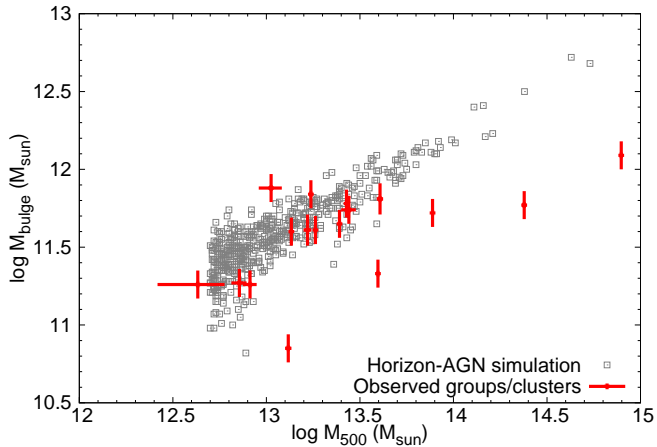


FIG. 7.— The relation between the stellar mass and the M_{500} mass for the 17 galaxy groups/clusters studied in this work and for the systems in the Horizon-AGN simulation. Note that the observed relation is notably flatter than the simulated one

sign a BH to a halo if it is within 10 per cent of the virial radius of the dark matter halo and to a halo+galaxy structure if the BH is also within twice the effective radius of the most massive galaxy within that halo. If more than one BH meets the criteria, the most massive BH is defined as the central BH (Volonteri et al. 2016).

The size of the box is $L_{\text{box}} = 100 h^{-1} \text{Mpc}$, and we identified 484 groups and clusters with M_{500} larger than $5 \times 10^{12} M_{\odot}$ at $z = 0$. In this paper, we analyze the central galaxy and respective BH for each group and cluster. We define the bulge mass as the total stellar mass.

5.2. Comparing the observed and simulated relations

We compare data and simulation in Figures 6 and 7. Simulation and data agree remarkably well in the $M_{\text{BH}} - M_{500}$ plane for the entire range of masses analyzed here (Figure 6 left panel). The scatter is also similar, albeit slightly lower ($\sigma_X = 0.20$ and $\sigma_Y = 0.19$) than that obtained for the observed sample.

The $M_{\text{BH}} - M_{\text{bulge}}$ relation, instead, shows several differences (Figure 6 right panel). The simulated galaxies have stellar masses reaching $5 \times 10^{12} M_{\odot}$, while observations are limited to $10^{12} M_{\odot}$. Additionally, the relation for simulated galaxies is much tighter. The tightness of the relation between BH mass and galaxy mass was already noticed in Volonteri et al. (2016), who argued that, although merger histories and environmental effects induce some scatter, unresolved internal process represent an important contribution to capturing the full scatter in the relationships.

For completeness, as in the case of observations, we compare M_{bulge} and M_{500} (Figure 7). Observations and the simulation agree well at $M_{500} < 3 \times 10^{13} M_{\odot}$, but in larger groups and in clusters, the stellar mass of simulated galaxies keeps rising steadily, while, as noted already for the $M_{\text{BH}} - M_{\text{bulge}}$ relation, in observations, galaxy mass seems to saturate at $\sim 10^{12} M_{\odot}$.

When comparing with simulations, we find that the Horizon-AGN simulation reproduces very well the observations in range explored here. If we extend the analysis to lower halo masses, considering only main halos and

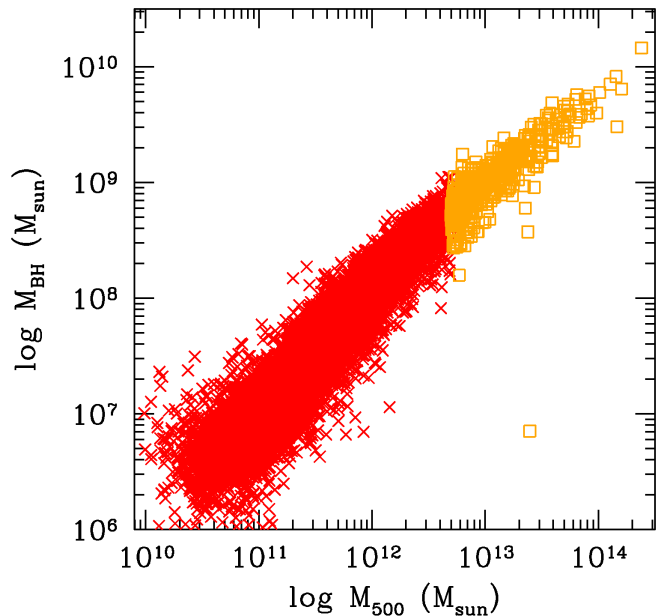


FIG. 8.— The relation between the stellar mass and the halo mass, in the Horizon-AGN simulation for all central galaxies in halos. BGGs/BCGs are shown as squares. The relation is shallower and tighter at the high-mass end (see Table 5).

TABLE 5
BEST-FIT PARAMETERS ON LINEAR REGRESSION FOR $M_{\text{BH}} - M_{500}$
IN THE SIMULATION

	α	β	σ
All halos	-1.23	0.77	0.42
$M_{500} < 2.5 \times 10^{12}$	-0.69	0.72	0.42
$M_{500} > 2.5 \times 10^{12}$	-1.22	0.78	0.18

not satellites (as satellites are affected by tidal stripping, see Volonteri et al. 2016), we find that the relation steepens slightly and scatter increases (Figure 8). If we fit separately the low- and high-mass ends with a divide at $M_{500} = 2.5 \times 10^{12}$, we find $\sigma = 0.42$ and $\sigma = 0.18$ respectively (see Table 5). As noted above for the relation with bulge mass, the Horizon-AGN simulation is likely to underestimate scatter at the low-mass end; therefore, the scatter found here is a lower limit. The limited correlation in late-type and bulgeless galaxies between BHs and dark matter halos (Kormendy & Bender 2011; Sun et al. 2013) may be an illustration of this effect.

5.3. Tight relation between the BH mass and total halo mass

Our conclusions, namely that the BH mass of BGGs/BCGs and the total mass of galaxy groups and clusters exhibit a tight relation, is similar to that obtained through the study of globular clusters. Specifically, Blakeslee (1997) suggested that the specific frequency of globular clusters in BCGs tightly correlates with the total mass of the host galaxy clusters. More recently, this conclusion was expanded for all types of

galaxies: Hudson et al. (2014) established that the mass ratio between globular clusters and the total halo is a constant ratio for every mass range. In addition, Burkert & Tremaine (2010) demonstrated that the specific frequency of globular clusters tightly correlate with the BH mass of galaxies. Combining these results implies that the mass of BHs are closely connected to the total halo mass of galaxies and for BCGs the BH mass and the total cluster mass are related.

In our sample of BGGs/BCGs, the BH mass appears to trace halo mass, via gas temperature, more tightly than the bulge mass. This suggests that the growth of the BHs in BGGs/BCGs may be indirectly governed by physical processes that are influenced by the large-scale potential of the host galaxy group or clusters. Such processes may be due to the inflow of cold gas onto the cluster center that directly feeds the BH, a series of low angular momentum mergers, or residual gas in the center of the galaxy after most of the gas was heated/expelled due to the quasar activity. To differentiate between these possibilities and to constrain the origin of the tight $M_{\text{BH}} - M_{500}$ relation, it will be essential to explore the evolutionary history of both the BGGs/BCGs and their host galaxy groups/clusters. However, such a dedicated study is beyond the scope of the present paper.

6. CONCLUSIONS

In this work, we explored the correlation between the BH mass of BGGs/BCGs and the properties of the host galaxy and group/cluster. Our results can be summarized as follows.

1. We analyzed *XMM-Newton* observations of 17 galaxy groups and clusters and measured their best-fit gas temperatures. The temperatures range from 0.347 – 8.165 keV, which corresponds to $M_{500} = (0.43 - 78.90) \times 10^{13} M_{\odot}$.

2. By utilizing dynamical BH mass measurements and the best-fit gas temperatures of the groups/clusters, we establish the $M_{\text{BH}} - kT$ relation, which exhibits a tight correlation with Pearson and Spearman correlation coefficients of 0.97 and 0.83, respectively.
3. We established the $M_{\text{BH}} - M_{\text{bulge}}$ relation, which exhibits large scatter and a Pearson and Spearman correlation coefficients of 0.70 and 0.35, respectively.
4. We conclude that for BHs residing in the centers galaxy groups and clusters, the scaling relation with the large-scale halo properties are significantly tighter than with the stellar bulge mass of the host galaxy. This suggests that the BH mass of BGGs/BCGs may be set by physical processes that are governed by the properties of the host galaxy cluster.
5. We compare the observed relations with those obtained in the Horizon-AGN simulation. We find that the overall slope of the relations are similar, albeit the simulated $M_{\text{BH}} - M_{\text{bulge}}$ exhibits significantly smaller scatter than the observed one.

Acknowledgements. We thank the referee for the careful review. This work uses observations obtained with *XMM-Newton*, an ESA science mission with instruments and contributions directly funded by ESA Member States and NASA. In this work, the NASA/IPAC Extragalactic Database (NED) have been used. Á.B. acknowledges support from the Smithsonian Institution. M.V. acknowledges funding from the European Research Council under the European Community's Seventh Framework Programme (FP7/2007-2013 Grant Agreement no. 614199, project BLACK).

REFERENCES

- Akritas, M. G., & Bershadsky, M. A. 1996, *ApJ*, 470, 706
 Arnaud, M., Pointecouteau, E., & Pratt, G. W. 2005, *A&A*, 441, 893
 Asplund, M., Grevesse, N., Sauval, A. J., & Scott, P. 2009, *ARA&A*, 47, 481
 Aubert D., Pichon C., Colombi S., 2004, *MNRAS*, 352, 376
 Bandara, K., Crampton, D., & Simard, L. 2009, *ApJ*, 704, 1135
 Beifiori, A., Courteau, S., Corsini, E. M., & Zhu, Y. 2012, *MNRAS*, 419, 2497
 Blakeslee, J. P. 1997, *ApJ*, 481, L59
 Blakeslee, J. P., Jordán, A., Mei, S., et al. 2009, *ApJ*, 694, 556
 Bogdán, Á., Forman, W. R., Zhuravleva, I., et al. 2012, *ApJ*, 753, 140
 Booth, C. M., & Schaye, J. 2010, *MNRAS*, 405, L1
 Burkert, A., & Tremaine, S. 2010, *ApJ*, 720, 516
 Cappellari, M., Verolme, E. K., van der Marel, R. P., et al. 2002, *ApJ*, 578, 787
 Dalla Bontà, E., Ferrarese, L., Corsini, E. M., et al. 2009, *ApJ*, 690, 537
 Dubois Y., Teyssier R., 2008, *A&A*, 477, 79
 Dubois Y., Devriendt J., Slyz A., Teyssier R., 2010, *MNRAS*, 409, 985
 Dubois Y., Devriendt J., Slyz A., Teyssier R., 2012, *MNRAS*, 420, 2662
 Dubois, Y., Pichon, C., Welker, C., et al. 2014, *MNRAS*, 444, 1453
 Dubois, Y., Volonteri, M., Silk, J., et al. 2015, *MNRAS*, 452, 1502
 Eckmiller, H. J., Hudson, D. S., & Reiprich, T. H. 2011, *A&A*, 535, A105
 Ferrarese, L., & Ford, H. C. 1999, *ApJ*, 515, 583
 Ferrarese, L. 2002, *ApJ*, 578, 90
 Ferré-Mateu, A., Mezcuca, M., Trujillo, I., Balcells, M., & van den Bosch, R. C. E. 2015, *ApJ*, 808, 79
 Freyberg, M. J., Pfeffermann, E., & Briel, U. G. 2006, The EPIC pn-CCD Detector Aboard XMM-Newton XMM-SOC-CAL-TN-0068
 Gebhardt, K., Bender, R., Bower, G., et al. 2000, *ApJ*, 539, L13
 Gebhardt, K., Adams, J., Richstone, D., et al. 2011, *ApJ*, 729, 119
 Gilfanov, M. 2004, *MNRAS*, 349, 146
 Gültekin, K., Richstone, D. O., Gebhardt, K., et al. 2009a, *ApJ*, 695, 1577
 Gültekin, K., Richstone, D. O., Gebhardt, K., et al. 2009b, *ApJ*, 698, 198
 Häring, N., & Rix, H.-W. 2004, *ApJ*, 604, L89
 Habouzit, M., Volonteri, M., Latif, M., et al. 2016, *MNRAS*, 456, 1901
 Hopkins, P. F., Hernquist, L., Cox, T. J., et al. 2006, *ApJS*, 163, 1
 Hudson, M. J., Harris, G. L., & Harris, W. E. 2014, *ApJ*, 787, L5
 Irwin, J. A., Athey, A. E., & Bregman, J. N. 2003, *ApJ*, 587, 356
 Kaviraj, S., Laigle, C., Kimm, T., et al. 2017, *MNRAS*, 467, 4739
 King, A. 2003, *ApJ*, 596, L27
 Hlavacek-Larrondo, J., Fabian, A. C., Edge, A. C., & Hogan, M. T. 2012, *MNRAS*, 424, 224
 Läscher, R., Ferrarese, L., van de Ven, G., & Shankar, F. 2014, *ApJ*, 780, 70
 Lovisari, L., Reiprich, T. H., & Schellenberger, G. 2015, *A&A*, 573, A118
 Kormendy, J., & Bender, R. 2011, *Nature*, 469, 377

- Kormendy, J., & Ho, L. C. 2013, *ARA&A*, 51, 511
- Magorrian, J., Tremaine, S., Richstone, D., et al. 1998, *AJ*, 115, 2285
- McConnell, N. J., Ma, C.-P., Gebhardt, K., et al. 2011, *Nature*, 480, 215
- McConnell, N. J., Ma, C.-P., Murphy, J. D., et al. 2012, *ApJ*, 756, 179
- McConnell, N. J., & Ma, C.-P. 2013, *ApJ*, 764, 184
- Nowak, N., Saglia, R. P., Thomas, J., et al. 2008, *MNRAS*, 391, 1629
- Omma H., Binney J., Bryan G., Slyz A., 2004, *MNRAS*, 348, 1105
- Pipino, A., Silk, J., & Matteucci, F. 2009, *MNRAS*, 392, 475
- Power C., Navarro J. F., Jenkins A., Frenk C. S., White S. D. M., Springel V., Stadel J., Quinn T., 2003, *MNRAS*, 338, 14
- Pratt, G. W., Croston, J. H., Arnaud, M., & Böhringer, H. 2009, *A&A*, 498, 361
- Rasera Y., Teyssier R., 2006, *A&A*, 445, 1
- Rusli, S. P., Thomas, J., Erwin, P., et al. 2011, *MNRAS*, 410, 1223
- Rusli, S. P., Thomas, J., Saglia, R. P., et al. 2013, *AJ*, 146, 45
- Savorgnan, G. A. D., & Graham, A. W. 2015, *MNRAS*, 446, 2330
- Schulze, A., & Gebhardt, K. 2011, *ApJ*, 729, 21
- Silk, J., & Rees, M. J. 1998, *A&A*, 331, L1
- Silk, J. 2005, *MNRAS*, 364, 1337
- Snowden, S. L., Mushotzky, R. F., Kuntz, K. D., & Davis, D. S. 2008, *A&A*, 478, 615
- Sun, A.-L., Greene, J. E., Impellizzeri, C. M. V., et al. 2013, *ApJ*, 778, 47
- Teyssier R., 2002, *A&A*, 385, 337
- Tonry, J. L., Dressler, A., Blakeslee, J. P., et al. 2001, *ApJ*, 546, 681
- Tully, R. B. 2015, *AJ*, 149, 171
- Tweed D., Devriendt J., Blaizot J., Colombi S., Slyz A., 2009, *A&A*, 506, 647
- van der Marel, R. P., & van den Bosch, F. C. 1998, *AJ*, 116, 2220
- Vika, M., Driver, S. P., Cameron, E., Kelvin, L., & Robotham, A. 2012, *MNRAS*, 419, 2264
- Vikhlinin, A., Kravtsov, A., Forman, W., et al. 2006, *ApJ*, 640, 691
- Volonteri, M., Dubois, Y., Pichon, C., & Devriendt, J. 2016, *MNRAS*, 460, 2979
- Volonteri, M., Natarajan, P., & Gültekin, K. 2011, *ApJ*, 737, 50
- Willingale, R., Starling, R. L. C., Beardmore, A. P., Tanvir, N. R., & O'Brien, P. T. 2013, *MNRAS*, 431, 394
- Wyithe, J. S. B., & Loeb, A. 2003, *ApJ*, 595, 614
- Zhang, Y.-Y., Reiprich, T. H., Finoguenov, A., Hudson, D. S., & Sarazin, C. L. 2009, *ApJ*, 699, 1178